npj | quantum materials

Article

Published in partnership with Nanjing University

https://doi.org/10.1038/s41535-024-00657-z

Higher order exchange driven noncoplanar magnetic state and large anomalous Hall effects in electron doped kagome magnet Mn_3Sn

Charanpreet Singh[1], Sk Jamaluddin[1], Subhadip Pradhan[1], Ashis K. Nandy[1], Masashi Tokunaga[2], Maxim Avdeev[3] & Ajaya K. Nayak[1]

Owing to geometrical frustration in the kagome lattice, Mn_3Sn displays a 120° in-plane triangular antiferromagnetic order, a manifestation of exchange interaction within the Heisenberg model. Here, we show the formation of a tunable noncoplanar magnetic ground state stabilized by higher-order exchange interactions in electron-doped Mn_3Sn samples. Our density Functional Theory calculations reveal that the higher-order exchange induces a partial out-of-plane alignment of the Mn moments, resulting in a canted magnetic state, further experimentally confirmed by neutron diffraction study along with 60 T magnetic and Hall resistivity measurements. Interestingly, we find a large scalar spin chirality-induced Hall signal depending on the degree of non-coplanarity of the Mn moments. Additionally, we demonstrate simultaneous manipulation of two-component order-parameter in the system, where the two Hall signals can be independently manipulated. The present study explores the quantum phenomena associated with the coexistence of multiple magnetic orders and their prospective use in spintronic devices.

In general, the origin of the magnetically ordered states can be understood by considering the exchange interactions using the Heisenberg model, which accounts for a variety of magnetic orders ranging from simple collinear to complex non-collinear magnetic states. However, the energy landscape of magnetic interactions is not limited to the usual pairwise Heisenberg exchange (J), instead higher-order exchange terms corresponding to multiple order of hopping between different sites can be taken into account in suitable magnetic systems. The most notable interaction involving multi-spins in a magnetic Hamiltonian is the 4-spin exchange in the form of 4-spin-two-site (B), 4-spin-three-site (Y), and 4-spin-four-site (K) interactions (Eq. (1))[1]. A signature feature of the 4-spin exchange interactions is the stabilization of multi-Q states. The noncoplanar 3Q magnetic ordering detected in Mn/Cu(111) system and the unique 2Q ground state observed in Fe/Rh(111) can be well explained by considering the 4-spin exchange interaction[2–5]. In addition, certain noncoplanar spin structures can be characterized by scalar spin chirality (SSC), defined as $S_i.(S_j \times S_k)$, which gives rise to an additional Hall response owing to the real space Berry phase. Such extraordinary Hall response has been previously observed in glassy systems[6–9] and a limited number of pyrochlore lattices[9–13].

The kagome lattice system, which can be constructed from the triangular lattice by removing one of the lattice points from the unit cell, exhibits a great prospect for the realization of various types of spin-ordering. Among them, Mn_3Sn is one of the extensively studied materials due to its multiple magnetic ordered states that include a 120° triangular antiferromagnetic (AFM) state. The cluster octupole order of the triangular AFM state breaks the time-reversal symmetry, resulting in the observation of Weyl nodes[14–17], which leads to the observation of large anomalous Hall effect in Mn_3Sn and Mn_3Ge[18–21]. In addition, the effect of cluster octupole order and/or Weyl nodes can also be seen from the realization of large spin/inverse spin Hall effect[22,23], electrical switching of Hall signal[24,25], and the Kondo effect[26], among others. Interestingly, Mn_3Sn displays a temperature-dependent modification of the magnetic ground state with different levels of electron doping[27–29]. However, the octupole order remains as the ground state at room temperature for all the electron-doped Mn_3Sn samples. Below the

[1]School of Physical Sciences, National Institute of Science Education and Research, An OCC of Homi Bhabha National Institute, Jatni, India. [2]The Institute for Solid-State Physics, University of Tokyo, Kashiwa, Chiba, Japan. [3]Australian Nuclear Science and Technology Organisation, Lucas Heights, NSW, Australia.
e-mail: ajaya@niser.ac.in

room temperature, the existence of a helical modulation of the triangular spin structure along the *c*-axis has been reported for the near stoichiometric Mn_3Sn samples[27,28,30]. For the higher electron-doped Mn_3Sn samples, the presence of a weakly ferromagnetic and glassy magnetic state was also reported, where the glassy nature comes from the additional Mn atoms occupying the Sn *2c* sites[31,32]. In addition, the possible existence of a canted magnetic structure at very low temperature is discussed in a recent report[33]. Furthermore, it has been reported that the electron doping in the form of Fe in place of Mn in $Mn_{3-x}Fe_xSn$ can stabilize a ferromagnetic-like low-temperature magnetic phase without a saturated magnetic state[34]. Similarly, Liu et al. reports the presence of magnetic bubbles in the nearly ferromagnetic sample $Mn_{2.1}Fe_{0.9}Sn$[35]. The existence of multiple magnetic ground states is also proposed in the polycrystalline $Mn_{2.5}Fe_{0.6}Sn_{0.9}$[36]. However, the exact nature and mechanism that governs the low-temperature magnetic phase and related transport phenomena remain unclear.

Results

Effect of higher-order exchange on the magnetic ground state of Mn_3Sn

The 120° triangular AFM ground state of Mn_3Sn can be derived from the *J* with in-plane magnetic anisotropy[30]. Possible higher-order exchange interactions along with the nearest neighbor Heisenberg exchange and corresponding hopping paths for Mn_3Sn are depicted in Fig. 1a. The Hamiltonian of the system with the 4-spin interactions can be written as,

$$H = \sum_{ij} J_{ij}(S_i.S_j) + \sum_{ij} B_{ij}(S_i.S_j)^2 + \sum_{ijk} Y_{ijk}[(S_i.S_j)(S_j.S_k) + (S_j.S_i)(S_i.S_k) + (S_i.S_k)(S_k.S_j)] + \sum_{ijkl} K_{ijkl}[(S_i.S_j)(S_k.S_l) + (S_i.S_l)(S_j.S_k) - (S_i.S_k)(S_j.S_l)]. \quad (1)$$

As discussed earlier, the magnetic ground state of Mn_3Sn can be effectively modified by a small electron doping. Motivated by these previous reports, we carry out a detailed first principle electronic calculation for the electron-doped Mn_3Sn samples. Using the virtual crystal approximation (VCA) technique as implemented in the Vienna Ab initio Simulation Package (VASP) code[37–40], we systematically vary the electron concentration by substituting Fe in place of Mn in $Mn_{3-x}Fe_xSn$. Starting from the in-plane 120° structure, we calculate the total energy of the pristine and the electron-doped samples by subjecting all the Mn moments with equal rotation from the kagome plane towards the c-axis, as represented in Fig. 1b. An in-depth examination concerning the calculation and the impact of various parameters can be found in Supplementary Figs. 18–28. The change in energy as a function of the out-of-plane canting angle ϕ is plotted in Fig. 1c. In the case

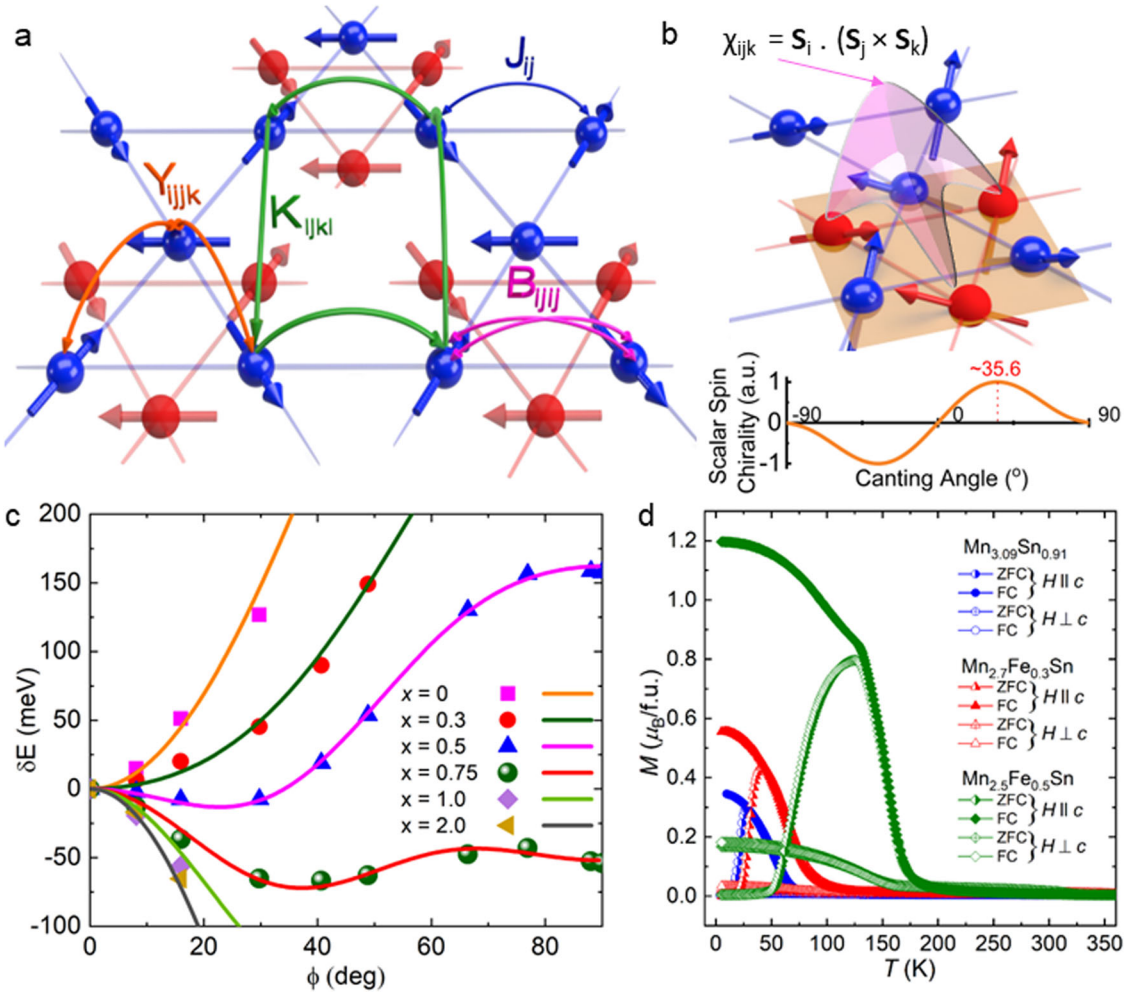

Fig. 1 | Higher-order magnetic interactions and scalar spin chirality. a Schematic diagram of the 120° in-plane triangular AFM structure of Mn_3Sn. The red and blue atoms represent two layers of kagome lattice formed by Mn atoms. Hopping paths for J_{ij}, B_{ij}, Y_{ijjk}, and K_{ijkl} are shown by blue, magenta, orange, and green curved arrows, respectively. **b** Schematic of an out-of-plane canted magnetic state with a finite scalar spin chirality (SSC), shown by the solid cone. The variation of SSC with canting angle is plotted at the bottom. **c** *abinitio* calculated change in energy (solid symbols) for $Mn_{3-x}Fe_xSn$ as a function of out-of-plane canting angle ϕ. The lines represent fittings with Eq. (1). **d** Temperature-dependent magnetization for $Mn_{3-x}Fe_xSn$ samples with field parallel and perpendicular to the c-axis.

of the undoped Mn_3Sn, we find a minimum at $\phi = 0$, signifying an in-plane triangular AFM order as the ground state. The calculated energy curve can be fitted only with the pairwise Heisenberg exchange term. A similar trend is found for $x = 0.3$, albeit the stability of the triangular AFM state ($\phi = 0°$) reduces significantly in comparison to the FM order ($\phi = 90°$). However, a satisfactory fit of the calculated energy for $x = 0.3$ can only be achieved with the inclusion of 4-spin exchange terms in addition to the 2-spin Heisenberg exchange.

By further increasing the electron doping in $x = 0.5$, a drastic change in the nature of the energy curve is observed where a shallow minimum appears at a finite value of the out-of-plane canting angle with $\phi = 23°$ [Fig. 1c]. The position of the minimum further increases to about $\phi = 37°$ for $x = 0.75$. For Fe doping beyond 1.0, the FM state comes out to be the ground state. Note that the end compound Fe_3Sn exhibits a FM ground state[41]. In contrast to the 3*Q* magnetic state with zero net magnetic moment found in the case of triangular lattice, here, the canted magnetic structure introduces a finite out-of-plane moment[2]. The energy curves for the intermediate Fe-doped samples are best fitted upon inclusion of 6-spin interaction in the form of $X_{ijk}(S_i.\ S_j)(S_j.\ S_k)(S_k.\ S_l)$ along with the 4-spin and 2-spin terms[42,43]. The extracted values of different order exchange constants from the fitting reveals that the canted magnetic ground state in the present case is stabilized by the higher order exchange contributions (Supplementary Fig. 26). The presence of effective higher order magnetic interactions in the local moment correlation functions in the Mn_3A based compounds is also mentioned by E. Mendive-Tapia et al. in their theoretical work[44]. It is worth mentioning that the in-plane component of the canted magnetic configuration can still retain the octupole order of the triangular AFM state[15,16]. The coexistence of this octupole order, along with the noncoplanar magnetic order stabilized by higher-order exchange can lead to a two-component order parameter in the system. The transport phenomena of such a magnetic ground state can be interesting. Motivated by our theoretical results, in this work, we experimentally demonstrate the existence of peculiar magnetic and AHE behaviors in the electron-doped $Mn_{3.09}Sn_{0.91}$ and $Mn_{3-x}Fe_xSn$ samples.

Low-temperature magnetic transition in electron-doped samples

The structural analysis of the present materials are summarized in Supplementary Fig. 1 and Supplementary Fig. 2. The temperature dependence of magnetization [$M(T)$] measured with field parallel and perpendicular to the c-axis for $Mn_{3.09}Sn_{0.91}$ and $Mn_{2.7}Fe_{0.3}Sn$, and $Mn_{2.5}Fe_{0.5}Sn$ are depicted in Fig. 1d (Supplementary Fig. 5). A distinguishable sharp upturn in the $M(T)$ data appears at low temperatures for all the samples when the field is applied parallel to the c-axis. On the contrary, the $M(T)$ curves for H⊥*c* show very low magnetization due to the near cancellation of the net magnetic moment in the *ab*-plane. The sudden increase in the magnetization at low temperatures for the H||*c* case indicates a realignment of the Mn moments along the c-axis. Most importantly, the temperature corresponding to this spin-reorientation transition (T_{SR}) and the out-of-plane magnetic moment increases gradually with Fe doping, signifying the stabilization of the out-of-plane magnetic state with Fe doping. It is worth mentioning that the T_{SR} for the undoped Mn_3Sn sample falls below 50 K[33], whereas $Mn_{2.5}Fe_{0.5}Sn$ exhibits T_{SR}=170 K that further increases to near room temperature for the polycrystalline $Mn_{2.3}Fe_{0.7}Sn$ sample (Supplementary Fig. 3). Further, the large irreversibility between the zero field cooled (ZFC) and the field cooled (FC) $M(T)$ curves for H||*c* indicates the presence of large out-of-plane magnetic anisotropy. The above results suggest the presence of an insurgent out-of-plane magnetic moment along with the in-plane triangular AFM state.

To further illustrate the stabilization of the out-of-plane magnetic state of the electron-doped Mn_3Sn samples, isothermal magnetization [$M(H)$] measurements are carried out at 5 K, as shown in Fig. 2(a-c). $M(H)$ plots for the full temperature range is shown in Supplementary Fig. 6. All three samples exhibit a large hysteretic behavior for the $M(H)$ loops measured with H||*c*, whereas linear kind of $M(H)$ curves are found for H⊥*c*. In addition, the saturation magnetization for H||*c* keeps on increasing and reaches a value of ≈2.0μ_B for $Mn_{2.5}Fe_{0.5}Sn$. In the case of the polycrystalline samples, the saturation magnetization further increases to ≈4.0μ_B for $Mn_{2.0}Fe_{1.0}Sn$ (Supplementary Fig. 3). It is important to note here that any increase in the in-plane magnetic moment of the Mn atoms with Fe doping cannot explain the large change in the out-of-plane magnetic moment below the T_{SR}. Moreover, a complete realignment of the Mn/Fe moments along the c-axis should give rise to a total moment of ~8μ_B/f.u. Hence, the systematic increase in the out-of-plane magnetic moment further corroborates the evolution of a canted magnetic state from the inverse triangular spin structure with electron doping.

Neutron diffraction experiment

To confirm the proposed non-coplanar magnetic ground state in the present system, we next carry out a temperature-dependent neutron diffraction (ND) study for the $Mn_{2.5}Fe_{0.5}Sn$ sample. The 350 K ND data recorded above the magnetic ordering temperature can be well fitted by considering the hexagonal Mn_3Sn structure. The magnetic structure at room temperature is found to be co-planar inverse triangular in nature. The 3 K ND data with Rietveld refinement using a non-coplanar model is shown in Fig. 2d. To analyze the low-temperature ND data, first we simulate the ND intensity considering the non-coplanar spin structure. The simulated patterns are obtained using the FullProf package, where the calculated intensities for different canting angles are exported. As it can be seen, an appreciable redistribution in the peak intensity only for the (200) and (201) reflections is found with increasing ϕ (Fig. 2e). Interestingly, the low-temperature ND data exhibit an exact trend to the simulated non-coplanar model, as shown in Fig. 2f. It can be clearly seen that the normalized integrated intensity of both (200) and (201) peaks starts increasing sharply at the onset of the T_{SR}. The enhanced intensities can only be accommodated by considering a non-coplanar canted model of the inverse triangular spin structure. For clarity, we have also plotted the zoomed view of the ND data along with fittings corresponding to the in-plane coplanar and the canted non-coplanar spin structures around (200) and (201) peaks at selected temperatures [Fig. 2g]. It can be seen that the observed intensities can only be fitted using a canted model below 150 K. The estimated canting angle at 3 K is about 16°, which decreases to zero at 150 K [inset of Fig. 2e]. The full range ND patterns at different temperatures with Rietveld analysis and other fitting parameters are shown in the Supplementary Figs. 9–16. For further clarity, we have also plotted the normalized integrated intensity of (100), (101), and (110) peaks showing a trivial increase in the intensity below the Neel temperature of the sample. In addition, we have also simulated the ND data by systematically increasing the Mn/Fe moment (Supplementary Fig. 15). As expected, the (200) peak does not show any intensity distribution, whereas the intensity of the (201) peak decreases with an increasing moment and hence can not account for the experimental findings. These results categorically establish that the non-coplanar magnetic state stabilized by out-of-plane canting of the Mn moments is the ground state in the electron-doped Mn_3Sn samples, hence, go hand in hand with our magnetization data and theoretical model. A small mismatch between the canting angle found experimentally and theoretically may arise due to slight correlation effects observed in the Mn_3Sn sample, where the best result was observed by using the DFT +DMFT calculations[45]. In addition, the spin triangles with and without Fe atom may show different canting angles. Interestingly, although the electron doping significantly modifies the low-temperature non-coplanar magnetic state, it does not introduce any kind of helical magnetic ordering in the system. We do not observe any satellite peaks expected for helical magnetic state in the neutron diffraction measurements. In addition, the presence of finite Hall signal over all the temperatures safely excludes the presence of helical phase.

Hall signal due to dual components of magnetic order

Next, we perform Hall resistivity measurements on our single crystalline samples in different geometries to uncover the effect of noncoplanar canted magnetic state on electron transport. Our magnetization measurements indicate that the in-plane 120° triangular AFM state remains robust

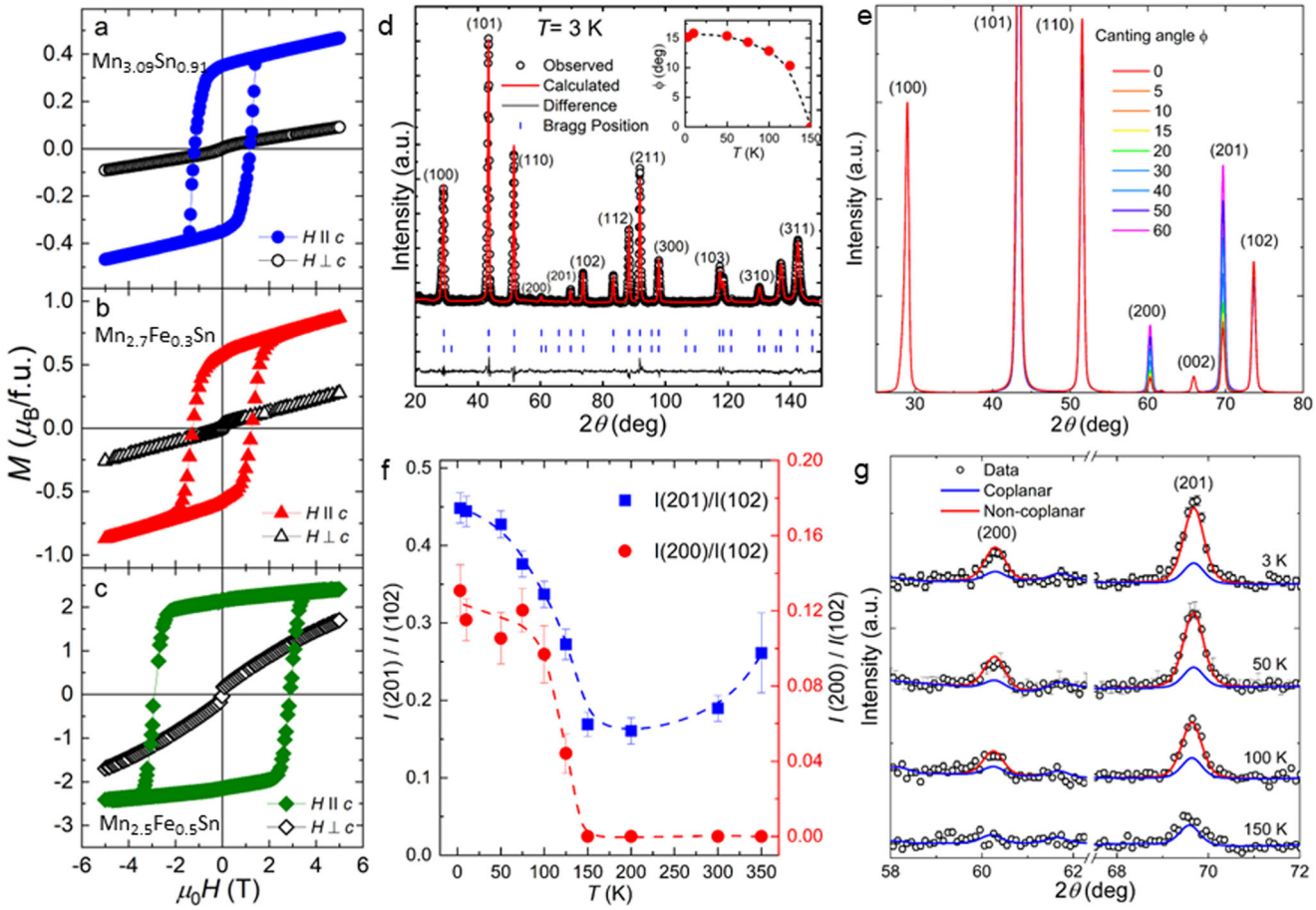

Fig. 2 | Magnetization and neutron diffraction study. Field dependent magnetization, $M(H)$, loops measured at 5 K with field parallel and perpendicular to the c-axis for (**a**) $Mn_{3.09}Sn_{0.91}$, **b** $Mn_{2.7}Fe_{0.3}Sn$, and **c** $Mn_{2.5}Fe_{0.5}Sn$ samples. **d** Rietveld refinement of the neutron diffraction (ND) pattern at 3 K for $Mn_{2.5}Fe_{0.5}Sn$. The data were recorded in a neutron wavelength $\lambda = 2.4395$ Å. We obtain the fitting parameter $R_{wp} = 11.3$ for the Rietveld refinement. The inset shows extracted canting angle at different temperatures. **e** Simulated powder neutron diffraction patterns corresponding to the out-of-plane canting of spins from the in-plane 120° structure for different canting angles ϕ. **f** Change in the relative integrated intensity of (200) and (201) peaks with respect to the (102) peak as a function of temperature. Dotted lines serve as a guide to the eye. **g** Expanded view of the (200) and (201) ND patterns at different temperatures, along with the Rietveld refinement for coplanar and noncoplanar models.

irrespective of the canting of the Mn moments. It is well known that the octupole domains of the in-plane AFM configuration align when a field is applied in the *ab*-plane[15]. The Hall voltage corresponding to this order can be observed in the ρ_{zx} component of the Hall resistivity. In addition, the formation of a canted magnetic state with Fe doping may give rise to a finite SSC, which in turn can generate an additional Hall signal that can be found from the ρ_{yx} measurement. Figure 3a–c show the ρ_{zx} and ρ_{yx} data measured at 5 K in a field up to 5 T. All the samples exhibit a robust ρ_{zx} signal that persists up to the magnetic ordering temperature (Supplementary Figs. 4 and 7), indicating the preservation of the octupole order. Most importantly, a large ρ_{yx} of about 14 μΩ-cm is also found for the $Mn_{3.09}Sn_{0.91}$ sample. With Fe doping, the ρ_{yx} increases to 25 μΩ-cm for $Mn_{2.7}Fe_{0.3}Sn$ and further surges to an extremely large ρ_{yx} of ≈ 35 μΩ-cm for $Mn_{2.5}Fe_{0.5}Sn$. We expect that the ρ_{yx} may attain its maxima for $Mn_{2.25}Fe_{0.75}Sn$ (Supplementary Fig. 4).

Independent switching of dual components of magnetic order

Although we have demonstrated that both ρ_{zx} and ρ_{yx} coexist in the electron-doped Mn_3Sn samples, it would be really interesting to study if these two different Hall signals in our samples can be manipulated simultaneously. For this purpose, we have performed AHE measurements on the $Mn_{2.7}Fe_{0.3}Sn$ single crystal by rotating the sample in a magnetic field. The measurement setup is prepared in such a way that both ρ_{zx} and ρ_{yx} can be measured at the same time (inset of Fig. 3d, right panel). First, the ρ_{yx} component of AHE is measured with $H \| c$ at 5 K, where a large SSC-induced AHE signal is clearly visible (Fig. 3d, middle panel). Subsequently, we set the ρ_{yx} to a positive maximum by applying a positive magnetic field before reducing the field to zero. In this configuration, we rotate the sample to apply in-plane magnetic fields ($H \perp c$) to measure the octupole order induced AHE, ρ_{zx}. At the same time, we also measure the spin chirality induced AHE, ρ_{yx}. As it can be seen from the left panel of Fig. 3d, the ρ_{zx} can be readily changed from positive to negative value by sweeping the in-plane magnetic fields while keeping the ρ_{yx} at the maximum value. The change in sign of the ρ_{zx} directly confirms a switching of the octupole order, whereas an unchanged ρ_{yx} signifies the preservation of the noncoplanar order. A similar kind of variation in the ρ_{zx} signal is observed by setting the ρ_{yx} at the negative maximum (Fig. 3d, right panel). These measurements clearly establish that the dual components of magnetic order can be individually manipulated using external stimuli.

Scaling of Hall resistivity with SSC

The observed ρ_{yx} component of the Hall resistivity can originate from the non-zero SSC induced by the non-coplanar magnetic ordering. The ρ_{yx} arising from the trivial out-of-plane magnetic moment must linearly vary with the magnetization. Whereas, the SSC-induced Hall signal depends on the canting angle of the Mn moments and exhibits oscillating nature, as shown in Fig. 1b. Hence, ρ_{yx} originating from the SSC must depend on the canting angle. Since the canting angle is maximum for $Mn_{2.5}Fe_{0.5}Sn$ among

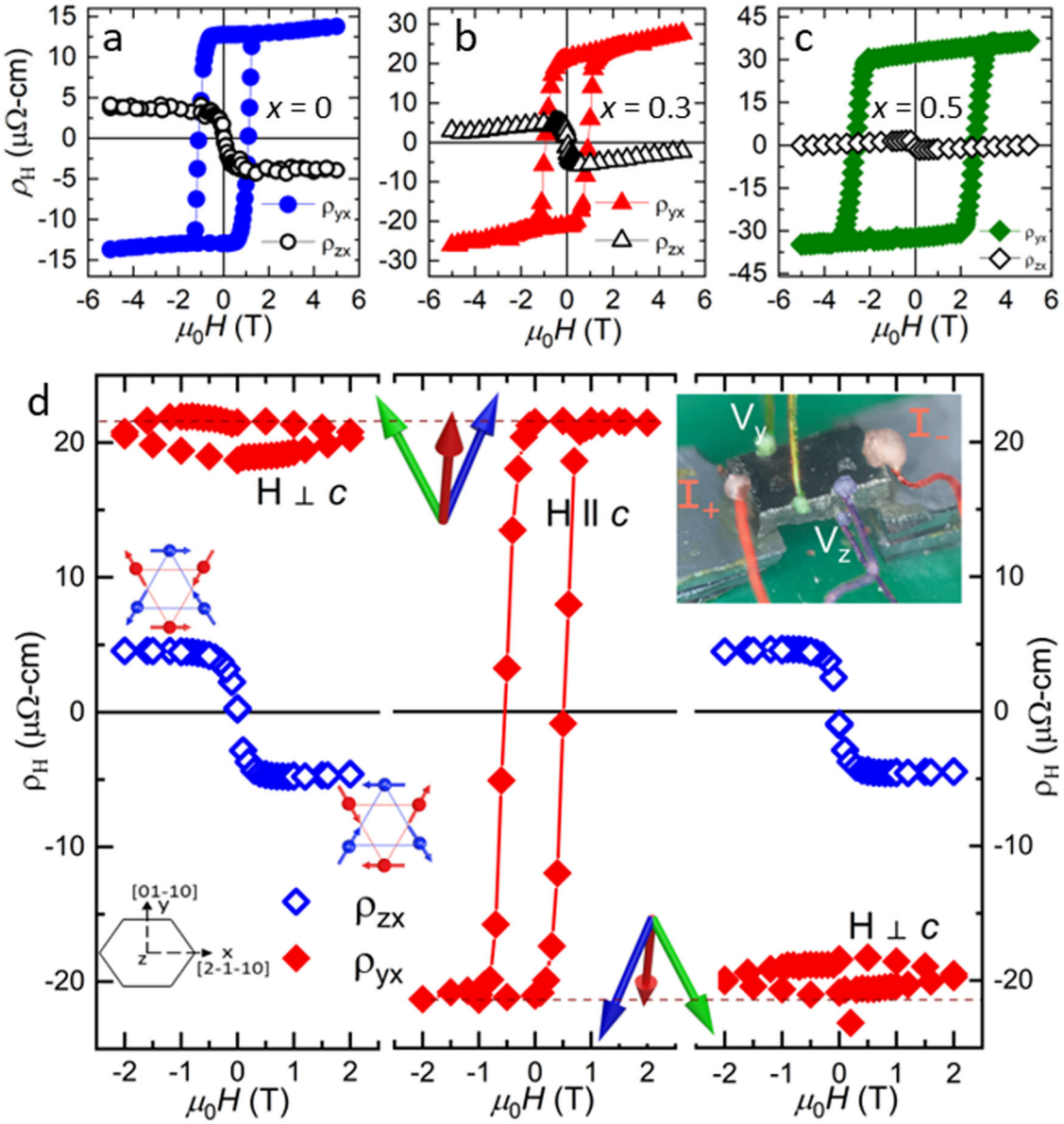

Fig. 3 | Individual manipulation of two component Hall voltage. Hall resistivity data, ρ_{yx} and ρ_{zx} for (**a**) $Mn_{3.09}Sn_{0.91}$, **b** $Mn_{2.7}Fe_{0.3}Sn$, and **c** $Mn_{2.5}Fe_{0.5}Sn$ samples measured at $T = 5$ K. **d** Individual switching of octupole and noncoplanar dipole orders for $Mn_{2.7}Fe_{0.3}Sn$ measured at 5 K. The middle panel represents ρ_{yx} with $H \| c$. The left and right panels show both ρ_{yx} and ρ_{zx} measurements with $H \perp c$. The image of the sample for the transport measurement is shown in the inset of the right panel.

the three single crystals that we present in this study, we carry out pulsed field magnetization and ρ_{yx} measurements up to 60 T on this sample, as shown in Fig. 4a, b. The magnetization of the sample increases monotonically with fields up to 60 T for all the measured temperatures (Fig. 4a), signifying a realignment of the Mn moments along the c-axis. This results in the change of canting angle from about 16° at zero field to ≈ 27° at 60 T for $T = 4.2$ K. Hence, we expect to see a dominating effect of SSC on the high field Hall data in comparison to the low field measurements.

The 60 T Hall resistivity (ρ_{yx}) measurement carried out on the $Mn_{2.5}Fe_{0.5}Sn$ sample is shown in Fig. 4b. The ρ_{yx} increases with the field and reaches a giant value of ≈ 50 μΩ-cm at 60 T for temperature between 4.2 K and 50 K. Most importantly, ρ_{yx} data exhibit a slower increase at higher fields compared to the magnetization data. This trend can be understood by invoking the SSC contribution to the Hall signal along with the trivial magnetization contribution According to the scaling relation, the Hall resistivity for the intrinsic contribution (as the present system falls in the bad metal regime) varies as : $\rho_{AHE} \propto \rho_{xx}^2 \times M$[9,46,47]. Figure 4c shows the fitting of ρ_{yx} with $\rho_{xx}^2 M$. It can be clearly seen that a good fitting is obtained at the low field range, whereas the fitting considerably deviates from the experimental data at very large fields for temperatures between 4.2 K and 100 K. This deviation at high fields (higher canting angle) originates due to the SSC contribution that becomes more nonlinear at higher canting angles. In contrast, a reasonable fitting of the experimental ρ_{yx} data is obtained at 150 K, where the zero field canting angle is almost negligible. This is also clear from the fact that the difference between the experimental data and the fitted curve is maximum at 4.2 K and decreases monotonically with increasing temperatures. To makes things more clear, we also plot ρ_{yx} as a function of SSC × ρ_{xx}^2 in Fig. 4d. In this case, a nice linear fitting is obtained for all temperatures up to 100 K, whereas the fitting deviates for 150 K. The slight mismatch in the fitting with SSC is due to the fact that although the SSC contributes predominately to the ρ_{yx} signal, a finite contribution from the trivial M component is always present. This is very clear from the fact that the experimental data can not be accounted with the SSC model at 150 K as it lies above the T_{SR} where Hall voltage is dominated by the trivial magnetization component. Hence, our high field measurements categorically establish that SSC is the major contributor to the ρ_{yx} component of the

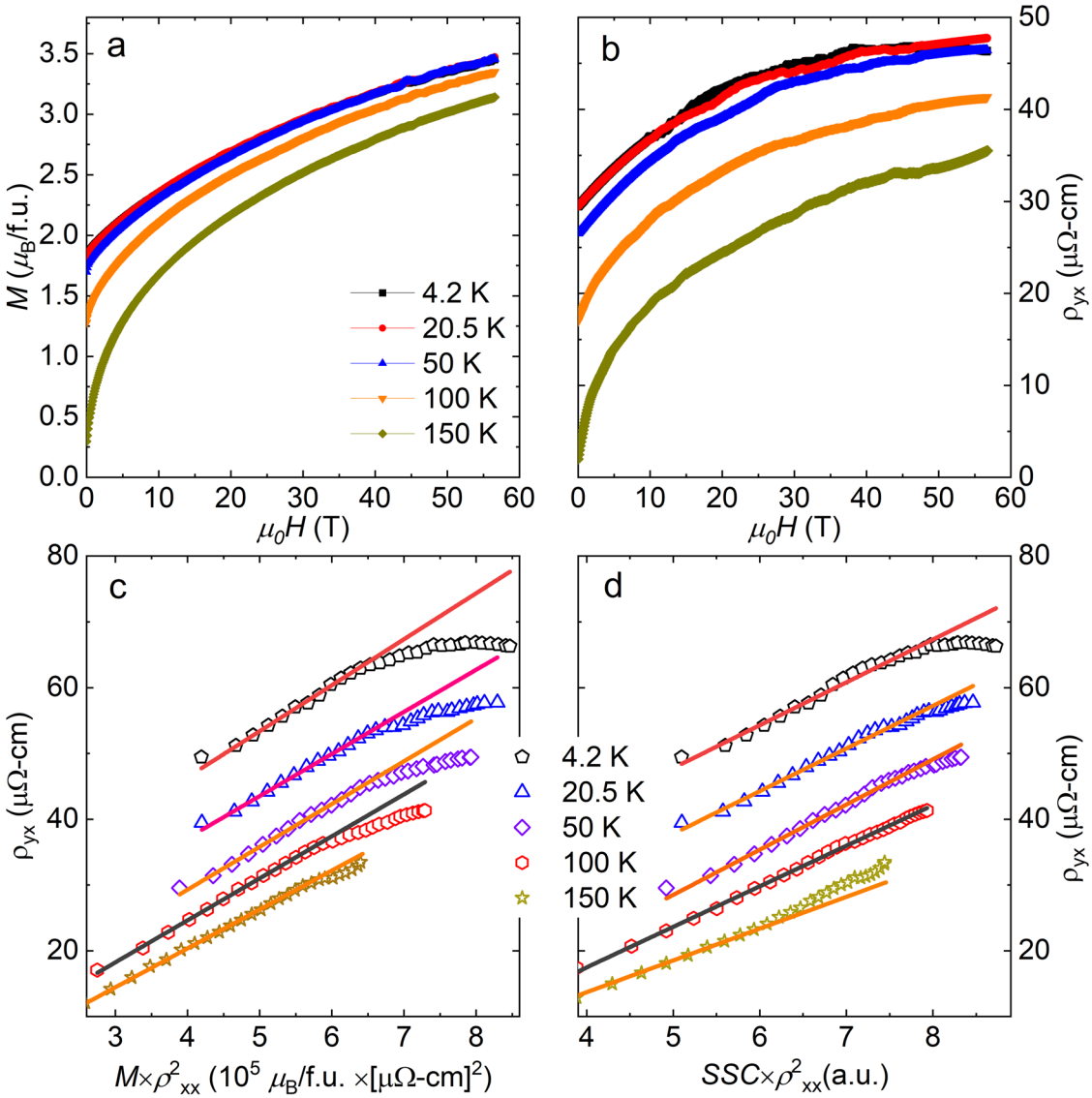

Fig. 4 | High field magnetic and Hall effect measurements. Field dependent (**a**) magnetization and **b** Hall resistivity data, ρ_{yx} measured for fields up to 60 T for $Mn_{2.5}Fe_{0.5}Sn$ sample. **c**, **d** Plot of ρ_{yx} against magnetization $M \times \rho_{xx}^2$, and SSC × ρ_{xx}^2. The lines represent a linear fit. The data in (**c**, **d**) is shifted along the *y*-axis for better clarity.

Hall resistivity. Refer to Supplementary Fig. 8 and Supplementary Fig. 17 for scaling of AHE with temperature.

Berry curvature due to noncoplanar magnetic state

In order to investigate the impact of the canted magnetic state on the electronic band structure, we carry out DFT calculations for both the in-plane triangular AFM structure with zero canting angle in Mn_3Sn and the canted non-coplanar magnetic state in $Mn_{2.5}Fe_{0.5}Sn$, as shown in Fig. 5. In case of $Mn_{2.5}Fe_{0.5}Sn$ the calculation is carried out for a canting angle of 25°. The plots also depict the regions of significant Berry curvature within the band structure. To facilitate a meaningful comparison, we specifically present the Berry curvature associated solely with the ρ_{yx} component. By examining the distribution of Berry curvature represented by the contrasting red and blue colors, it becomes apparent that there are minimal regions of significant Berry curvature for Mn_3Sn. This limited presence of Berry curvature naturally leads to a vanishing anomalous Hall conductivity (AHC), as clearly demonstrated in Fig. 5c. Notably, only a finite value of the σ_{zx} component is observed at the Fermi level, which is in line with our experimental findings for the in-plane magnetic structure, as illustrated in Supplementary Fig. 3. In contrast, the band structure of the $Mn_{2.5}Fe_{0.5}Sn$ with a canting angle of 25° exhibits a noteworthy variation in comparison to that of Mn_3Sn. Notably, the previously discussed topological characteristics, often associated with a Weyl semimetal, are absent from the band structure of the canted system. However, a distinct enhancement in the Berry curvature, specifically in the ρ_{yx} component of Hall resistivity, becomes evident. This augmentation is clearly illustrated in Fig. 5d, where we present the corresponding calculated AHC. As anticipated, a substantial value of σ_{yx} is observed at the Fermi level, accompanied by a small σ_{zx} component. Remarkably, this outcome corroborates our experimental findings (Fig. 3c), where a significant Hall signal is observed in the ρ_{yx} and a very small value is seen for ρ_{zx} component. Hence, a direct correlation is established between our experimental observations and the corresponding theoretical calculations[17,20]. The high magnetic field Hall resistivity measurements also provide evidence of the SSC nature of the Hall signal. Furthermore, recent calculations by Li et al.[48] also reinforce our interpretation, indicating a mechanism driven by scalar spin chirality, rather than spin-orbit coupling, as the underlying cause of the Hall signal found in the present system.

Discussion

After the discovery of large AHE in the triangular AFM state of Mn_3Sn, a considerable amount of work has been carried out related to the role of underlying magnetic structure in determining the band topology in the

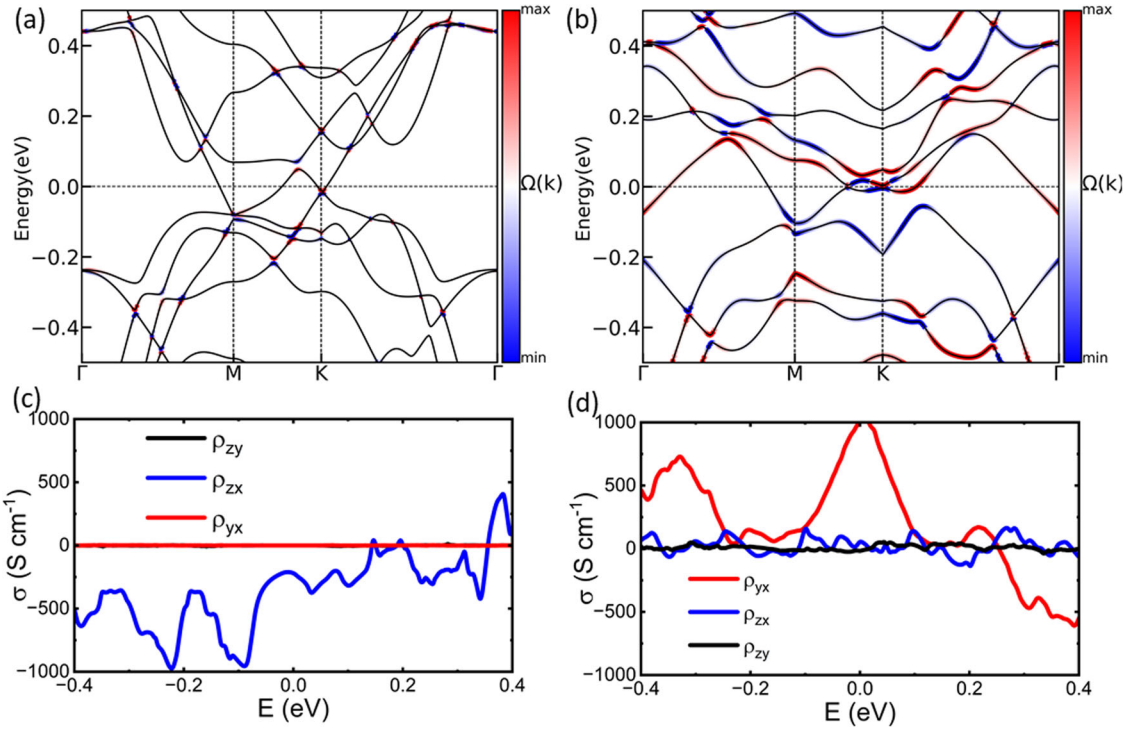

Fig. 5 | Theoretical calculations of band structure and anomalous Hall conductivity. DFT calculated band struture for (**a**) in-plane triangular AFM structure of Mn_3Sn and **b** canted non-coplanar structure for $Mn_{2.5}Fe_{0.5}Sn$ systems. The color shows the Berry curvature. The anomalous Hall conductivity as a function of energy for (**c**) in-plane triangular AFM structure of Mn_3Sn and **d** canted non-coplanar structure for $Mn_{2.5}Fe_{0.5}Sn$ systems. Fermi level is taken as $E = 0$.

system[17,30,49]. In all the cases, the magnetic properties of the system can be understood by invoking the 2-spin exchange interaction. It is also well known that the non-zero intra-plane Dzyaloshinskii-Moriya interaction (DMI) dictates the sense of rotation of the spins in the octupole magnetic structure and leads to the inverse triangular spin structure in Mn_3Sn. As our samples exhibit the octupole order-induced Hall signal for all levels of doping in whole temperature range, it can be concluded that the role of DMI does not change in the present electron-doped Mn_3Sn system. Furthermore, the centrosymmetric nature of the samples safely exclude any inter-plane DMI in the system. Hence, the present work brings foreward a different direction in the understanding of the role of higher-order interaction to stabilize the non-coplanar magnetic ground state. For the present layered kagome lattice structure, the 4-spin and 6-spin terms stabilize a tunable noncoplanar spin structure with dual order characteristics. This magnetic state gives rise to a large Hall signal related to the real space Berry curvature of the system. At the same time, the momentum space Berry curvature induced AHE can be independently manipulated without affecting the former one. This exemplifies the rich Berry phase physics of the underlying electron band structure in the electron-doped Mn_3Sn system. Hence in this direction, it would be really interesting to study the effect of multi-spin interaction to the band topology of the present class of materials.

Moreover, the present finding of non-coplanar magnetic structure adds several opportunities to the possible room temperature applications of the triangular AFM-based non-collinear magnetic states in Mn_3Sn. One of the most striking effects that can be easily manipulated is the finite real-space Berry curvature associated with the scalar spin chirality (SSC). This non-vanishing SSC can generate a large anomalous Hall signal even in the absence of any spin-orbit coupling (SOC). The extremely large AHE (ρ_{yx}) realized in the present case belongs to this category. Furthermore, these noncoplanar states have also been proposed to induce topological superconductivity when proximitized to trivial s-wave superconductors[50]. Hence, it can be safely proposed that the non-coplanar magnetic states are potential substitutes to the SOC-based AHE. Furthermore, the observation of two different sources for the present AHE is a consequence of the non-coplanar magnetic ordering in the system. Due to this dual nature of the order parameter, a storage unit in a memory device can be proposed with larger than one bit. This is similar to the multi-level cell in modern SSD storages, where one unit can store more states, such as [0, 0][0, 1][1, 0][1, 1] instead of normal [0][1]. In addition, the non-coplanar magnetic ground state stabilized by the higher-order exchange interactions, mostly ignored previously, could play a prevalent role in several other similar materials in the future studies.

In conclusion, the present study exemplifies the effects of higher order exchanges in the stabilization of ground state properties of the layered kagome lattice-based electron-doped Mn_3Sn. A canted magnetic state is expected to play the primary role in the realization of a large anomalous Hall signal of topological origin. In addition to the noncoplanar magnetic state, the octupole order of the layered kagome structure can be preserved for all the samples. This results in a dual magnetic order, where both these orders can be manipulated individually using magnetic fields. We hope that the present results will motivate further studies on the effect of higher-order interactions on a variety of lattice classes. In addition, prospective device application of the dual order system can be anticipated.

Note: During the review process of the present manuscript, we came across a manuscript by Li et al.[48], which discusses the modification of the electronic band structure due to a very small canting induced by the magnetic field. Our study presents a comprehensive study on the intrinsics-canted magnetic ground state itself in the electron-doped Mn_3Sn system.

Methods

Single-crystal growth and characterization

Polycrystalline samples of $Mn_{3-x}Fe_xSn$ were synthesized by arc melting the stoichiometric amount of high-purity constituent elements. Later, the samples were sealed in high vacuum quartz tubes and annealed at 800 °C for eight days. To synthesize single crystals, the polycrystalline samples were powdered and sealed under a high vacuum in pointed alumina crucibles. Then the samples were heated to above the melting point and slowly cooled down to ~800 °C. Single crystals of size ~3–4 mm were found to crystallize

in the case of $Mn_{3.09}Sn_{0.91}$, whereas smaller size crystals were found for the Fe-doped samples. The structural phase of the samples was determined by room temperature powder X-ray diffraction (XRD) using Cu-K_α radiation (Rigaku) (Supplementary Fig. 1). The composition and homogeneity of the samples were determined by field emission scanning electron microscopy (FESEM), energy dispersive X-ray spectroscopy (EDS). The Electron Backscatter Diffraction (EBSD) characterization was used to confirm the single crystalline nature of samples (Supplementary Fig. 2).

Magnetic and transport measurements

Magnetic measurements were carried out using vibrating sample SQUID magnetometer (MPMS-3, Quantum Design). Transport measurements were carried out using Quantum Design Physical Properties Measurement System (PPMS). Powder neutron diffraction measurements were performed at the High Resolution Powder Diffractometer - Echidna[51], housed at ANSTO, Australia, with a neutron wavelength of 2.4395 Å. The data analysis was performed with the FullProf Suite[52]. High-magnetic-field transport and magnetic measurements up to 60 T were performed at the International MegaGauss Science Laboratory of the Institute for Solid State Physics (ISSP), University of Tokyo.

Density functional theory calculations

The density functional theory (DFT) calculations are employed to study the magnetic properties of the system. The spin-polarized calculations have been carried out within the projector augmented wave (PAW) method[53] as implemented in Vienna Ab initio Simulation Package (VASP)[37–40]. The generalized gradient approximation (GGA)is used as the exchange-correlation potential in the form of Perdew-Burke-Enzerhof (PBE)[54]. For the Brillouin-Zone (BZ) integration, a Γ-centered k-point grid of $8 \times 8 \times 9$ is used with a plane-wave cut-off energy of 500 eV. The virtual crystal approximation (VCA) technique, as implemented in the Vienna Ab initio Simulation Package (VASP) code, is used to calculate the effect of Fe doping in $Mn_{3-x}Fe_xSn$ system.

The DFT calculations for the band structure were performed using full-potential linearized augmented plane wave (FLAPW) method as implemented in the FLEUR code (www.flapw.de). To expand the LAPW basis functions, a plane-wave cutoff of $k_{max} = 4.2$ a.u.$^{-1}$ was employed. Additionally, a Monkhorst-Pack k-mesh of $8 \times 8 \times 9$ was utilized to cover the Brillouin zone (BZ). The tight-binding Hamiltonian was constructed by considering atomic orbital-like maximally-localized Wannier functions (MLWFs) derived from Mn-d, Fe-d and Sn-p states using the Wannier90 tool[55,56] using a grid of $8 \times 8 \times 9$. Subsequently, the WannierBerri Python code[57] was employed to calculate the anomalous Hall conductivity (AHC) and map the Berry curvature onto the band structure. The AHC calculations were performed employing a highly dense grid of $500 \times 500 \times 500$ points.

Data availability

All data used to obtain the conclusions in this paper are presented in the paper and/or the Supplementary Materials. Other data may be requested from the authors. Please direct all inquiries to A.K.N. (ajaya@niser.ac.in).

Received: 15 September 2023; Accepted: 9 May 2024;
Published online: 22 May 2024

References

1. Adler, J. & Oitmaa, J. The Heisenberg ferromagnet with higher-order exchange. *J. Phys. C.* **12**, 575 (1979).
2. Kurz, P., Bihlmayer, G., Hirai, K. & Blügel, S. Three-dimensional spin structure on a two-dimensional lattice: Mn/Cu(111). *Phys. Rev. Lett.* **86**, 1106 (2001).
3. Krönlein, A. Magnetic ground state stabilized by three-site interactions: Fe/Rh(111). *Phys. Rev. Lett.* **120**, 207202 (2018).
4. Spethmann, J. et al. Discovery of magnetic single- and triple-q states in Mn/Re(0001). *Phys. Rev. Lett.* **124**, 227203 (2020).
5. Hoffmann, M. & Blügel, S. Systematic derivation of realistic spin models for beyond-Heisenberg solids. *Phys. Rev. B* **101**, 024418 (2020).
6. Kawamura, H. Anomalous Hall effect as a probe of the chiral order in spin glasses. *Phys. Rev. Lett.* **90**, 047202 (2003).
7. Taniguchi, T. et al. Direct observation of chiral susceptibility in the canonical spin glass AuFe. *Phys. Rev. Lett.* **93**, 246605 (2004).
8. Pureur, P., Fabris, F. W., Schaf, J. & Campbell, I. A. Chiral susceptibility in canonical spin glass and re-entrant alloys from Hall effect measurements. *Europhys. Lett.* **67**, 123 (2004).
9. Nagaosa, N., Sinova, J., Onoda, S., MacDonald, A. H. & Ong, N. P. Anomalous hall effect. *Rev. Mod. Phys.* **82**, 1539 (2010).
10. Taguchi, Y., Oohara, Y., Yoshizawa, H., Nagaosa, N. & Tokura, Y. Spin chirality, Berry phase, and anomalous Hall effect in a frustrated ferromagnet. *Science* **291**, 2573 (2001).
11. Taguchi, Y. et al. Magnetic field induced sign reversal of the anomalous Hall effect in a pyrochlore ferromagnet $Nd_2Mo_2O_7$: evidence for a spin chirality mechanism. *Phys. Rev. Lett.* **90**, 257202 (2003).
12. Fabris, F. W., Pureur, P., Schaf, J., Vieira, V. N. & Campbell, I. A. Chiral anomalous Hall effect in reentrant AuFe alloys. *Phys. Rev. B* **74**, 214201 (2006).
13. Machida, Y., Nakatsuji, S., Onoda, S., Tayama, T. & Sakakibara, T. Time-reversal symmetry breaking and spontaneous Hall effect without magnetic dipole order. *Nature* **463**, 210 (2010).
14. Nomoto, T. & Arita, R. Cluster multipole dynamics in noncollinear antiferromagnets. *Phys. Rev. Res.* **2**, 012045 (2020).
15. Higo, T. et al. Large magneto-optical Kerr effect and imaging of magnetic octupole domains in an antiferromagnetic metal. *Nat. Photon.* **12**, 73 (2018).
16. Kimata, M. et al. X-ray study of ferroic octupole order producing anomalous Hall effect. *Nat. Commun.* **12**, 5582 (2021).
17. Yang, H. et al. Topological Weyl semimetals in the chiral antiferromagnetic materials Mn_3Ge and Mn_3Sn. *N. J. Phys.* **19**, 015008 (2017).
18. Nayak, A. K. et al. Large anomalous Hall effect driven by a nonvanishing Berry curvature in the noncolinear antiferromagnet Mn_3Ge. *Sci. Adv.* **2**, e1501870 (2016).
19. Nakatsuji, S., Kiyohara, N. & Higo, T. Large anomalous Hall effect in a non-collinear antiferromagnet at room temperature. *Nature* **527**, 212 (2015).
20. Chen, T. et al. Anomalous transport due to Weyl fermions in the chiral antiferromagnets Mn3X, X = Sn, Ge. *Nat. Commun.* **12**, 572 (2021).
21. Pradhan, S., Samanta, K., Saha, K. & Nandy, A. K. Vector-chirality driven topological phase transitions in noncollinear antiferromagnets and its impact on anomalous Hall effect. *Commun. Phys.* **6**, 272 (2023).
22. Kimata, M. et al. Magnetic and magnetic inverse spin Hall effects in a non-collinear antiferromagnet. *Nature* **565**, 627–630 (2019).
23. Železnyˇ, J., Zhang, Y., Felser, C. & Yan, B. Spin-polarized current in noncollinear antiferromagnets. *Phys. Rev. Lett.* **119**, 187204 (2017).
24. Tsai, H. et al. Electrical manipulation of a topological antiferromagnetic state. *Nature* **580**, 608–613 (2020).
25. Higo, T. et al. Perpendicular full switching of chiral antiferromagnetic order by current. *Nature* **607**, 474–479 (2022).
26. Khadka, D. et al. Kondo physics in antiferromagnetic Weyl semimetal $Mn_{3+x}Sn_{1-x}$ films. *Sci. Adv.* **6**, eabc1977 (2020).
27. Sung, N. H. et al. Comparing the anomalous Hall effect and the magneto-optical Kerr effect through antiferromagnetic phase transitions in Mn_3Sn. *Appl. Phys. Lett.* **112**, 132406 (2018).
28. Singh, C. et al. Pressure controlled trimerization for switching of anomalous Hall effect in triangular antiferromagnet Mn_3Sn. *Phys. Rev. Res.* **2**, 043366 (2020).
29. Ikhlas, M., Tomita, T. & Nakatsuji, S. Sample quality dependence of the magnetic properties in non-collinear antiferromagnet Mn_3Sn. *JPS Conf. Proc.* **30**, 011177 (2020).
30. Park, P. et al. Magnetic excitations in non-collinear antiferromagnetic Weyl semimetal Mn_3Sn. *npj Quant. Mater.* **3**, 63 (2018).

31. Tomiyoshi, S., Abe, S., Yamaguchi, Y., Yamauchi, H. & Yamamoto, H. Triangular spin structure and weak ferromagnetism of Mn_3Sn at low temperature. *J. Magn. Magn. Mater.* **54**, 1001 (1986).
32. Feng, W. J. et al. Glassy ferromagnetism in Ni_3Sn-type Mn_3. $1Sn_{0.9}$. *Phys. Rev. B* **73**, 205105 (2006).
33. Rout, P. K., Madduri, P. P., Manna, S. K. & Nayak, A. K. Field-induced topological Hall effect in the noncoplanar triangular antiferromagnetic geometry of Mn_3Sn. *Phys. Rev. B* **99**, 094430 (2019).
34. Felez, M. R., Coelho, A. A. & Gama, S. Magnetic properties of $Mn_{3-x}Fe_xSn$ compounds with tuneable Curie temperature by Fe content for thermomagnetic motors. *J. Magn. Magn. Mater.* **444**, 280 (2017).
35. Liu, J. et al. Spontaneous magnetic bubbles and large topological Hall effect in Mn $_{3-x}$ Fe_x Sn compound. *Scr. Mater.* **187**, 268 (2020).
36. Liu, Z. H. et al. Evolution of diverse Hall effects during the successive magnetic phase transitions in Mn_2. $5Fe_{0.6}Sn_{0.9}$. *J. Phys.: Condens. Matter* **33**, 115803 (2021).
37. Kresse, G. & Hafner, J. *Abinitio* molecular dynamics for liquid metals. *Phys. Rev. B* **47**, 558 (1993).
38. Kresse, G. & Hafner, J. *Abinitio* molecular-dynamics simulation of the liquid-metal-amorphous-semiconductor transition in germanium. *Phys. Rev. B* **49**, 14251 (1994).
39. Kresse, G. & Furthmüller, J. Efficient iterative schemes for *abinitio* total-energy calculations using a plane-wave basis set. *Phys. Rev. B.* **54**, 11169 (1996).
40. Kresse, G. & Furthmüller, J. Efficiency of ab-initio total energy calculations for metals and semiconductors using a plane-wave basis set. *Comput. Mater. Sci.* **6**, 15 (1996).
41. Sales, B. C., Saparov, B., McGuire, M. A., Singh, D. J. & Parker, D. S. Ferromagnetism of Fe_3Sn and alloys. *Sci. Rep.* **4**, 7024 (2014).
42. Grytsiuk, S. Topological-chiral magnetic interactions driven by emergent orbital magnetism. *Nat. Commun.* **11**, 511 (2020).
43. Brinker, S., dos Santos Dias, M. & Lounis, S. Prospecting chiral multisite interactions in prototypical magnetic systems. *Phys. Rev. Res.* **2**, 033240 (2020).
44. Mendive-Tapia, E. & Staunton, J. B. Ab initio theory of the Gibbs free energy and a hierarchy of local moment correlation functions in itinerant electron systems: The magnetism of the Mn_3A materials class. *Phys. Rev. B* **99**, 144424 (2019).
45. Yu, T. et al. Correlated electronic structure of the kagome metal Mn_3Sn. *Phys. Rev. B* **106**, 205103 (2022).
46. Zeng, C., Yao, Y., Niu, Q. & Weitering, H. H. Linear magnetization dependence of the intrinsic anomalous Hall effect. *Phys. Rev. Lett.* **96**, 037204 (2006).
47. Wang, Q. et al. Large intrinsic anomalous Hall effect in half-metallic ferromagnet $Co_3Sn_2S_2$ with magnetic Weyl fermions. *Nat. Commun.* **9**, 3681 (2018).
48. Li, X., Koo, J., Zhu, Z., Behnia, K. & Yan, B. Field-linear anomalous Hall effect and Berry curvature induced by spin chirality in the kagome antiferromagnet Mn_3Sn. *Nat. Commun.* **14**, 1642 (2023).
49. Kübler, J. & Felser, C. Weyl fermions in antiferromagnetic Mn_3Sn and Mn_3Ge. *Europhys. Lett.* **120**, 47002 (2018).
50. Bedow, J. et al. Topological superconductivity induced by a triple-q magnetic structure. *Phys. Rev. B* **102**, 180504 (2020).
51. Avdeev, M. & Hester, J. R. ECHIDNA: a decade of high-resolution neutron powder diffraction at OPAL. *J. Appl. Crystallogr.* **51**, pp.1597-1604 (2018).
52. Rodriguez-Carvajal, J. *Physica B: Condensed Matter.* Vol. **192** (1-2), p. 55–6 (1993).
53. Blöchl, P. E. Projector augmented-wave method. *Phys. Rev. B* **50**, 17953 (1994).
54. Perdew, J. P., Burke, K. & Ernzerhof, M. Generalized gradient approximation made simple. *Phys. Rev. Lett.* **77**, 3865 (1996).
55. Marzari, N., Mostofi, A. A., Yates, J. R., Souza, I. & Vanderbilt, D. Maximally localized Wannier functions: theory and applications. *Rev. Mod. Phys.* **84**, 1419–1475 (2012).
56. Mostofi, A. A. et al. An updated version of Wannier90: a tool for obtaining maximally-localised Wannier functions. *Comput. Phys. Commun.* **185**, 2309–2310 (2014).
57. Tsirkin, S. S. High performance Wannier interpolation of Berry curvature and related quantities with WannierBerri code. *npj Comput. Mater.* **7**, 33 (2021).

Acknowledgements

A.K. Nayak acknowledges the Department of Atomic Energy (DAE), the Department of Science and Technology (DST)-Ramanujan research grant (No. SB/S2/RJN-081/2016) and SERB research grant (ECR/2017/000854) of the Government of India for financial support. A.K.Nandy acknowledges the support of DAE and SERB research grant (Grant No. SRG/2019/000867) of the Government of India. The theoretical computations have been performed on KALINGA high-performance computing facility at NISER, Bhubaneswar. A.K. Nayak thanks Amitabh Das, Bhabha Atomic Research Centre, Mumbai, for recording the initial neutron diffraction data and its preliminary analysis.

Author contributions

A.K. Nayak conceived the idea of the present work and led the project. C.S. prepared the single crystalline and polycrystalline samples and carried out the low-field magnetic and transport measurements. The single crystal characterization was performed by S.J.; C.S. performed the theoretical calculation along with A.K. Nandy.; M.T. performed the pulse field magnetization and transport measurements. M.A. carried out the neutron diffraction measurements. All authors contribute to the data analysis. C.S. and A.K. Nayak wrote the manuscript.

Competing interests

The authors declare no competing interests.

Additional information

Supplementary information The online version contains supplementary material available at https://doi.org/10.1038/s41535-024-00657-z.

Correspondence and requests for materials should be addressed to Ajaya K. Nayak.